RESEARCH ARTICLE
SPACE PHYSICS

*Earth and Planetary Physics*
*7*: 548–557, 2023
doi: 10.26464/epp2023071

# Horizontal structure of convergent wind shear associated with sporadic E layers over East Asia

**LiHui Qiu[1,3], Xian Lu[2], Tao Yu[1]*, Yosuke Yamazaki[3], HuiXin Liu[4], Yang-Yi Sun[1], HaoNan Wu[2], XiaoMin Zuo[5], XiangXiang Yan[1], Yan Yu[1], and YiFan Qi[1]**

[1]Institute of Geophysics & Geomatics, China University of Geosciences, Wuhan 430074, China;

[2]Department of Physics and Astronomy, Clemson University, Clemson, SC 29631, USA;

[3]Leibniz institute of Atmospheric Physics at the University of Rostock, 18225 Kühlungsborn, Germany;

[4]Department of Earth and Planetary Sciences, Kyushu University, Fukuoka 8190395, Japan;

[5]School of Mathematics and Physics, China University of Geosciences, Wuhan 430074, China

**Key Points:**

- The simulation produces the horizontal structure of the ion convergence region (HSICR).
- The shapes of HSICRs show a typical frontal structure elongated in northwest–southeast and/or northeast–southwest.
- HSICR can reveal and explain the shapes of the large-scale Es layers.

**Citation:** Qiu, L. H., Lu, X., Yu, T., Yamazaki, Y., Liu, H. X., Sun, Y.-Y., Wu, H. N., Zuo, X. M., Yan, X. X., Yu, Y., and Qi, Y. F. (2023). Horizontal structure of convergent wind shear associated with sporadic E layers over East Asia. *Earth Planet. Phys.*, *7*(5), 548–557. http://doi.org/10.26464/epp2023071

**Abstract:** At present, the main detection instruments for observing sporadic E (Es) layers are ground-based radars, dense networks of ground-based global navigation satellite system (GNSS) receivers, and GNSS radio occultation, but they cannot capture the whole picture of the horizontal structure of Es layers. This study employs the Whole Atmosphere Community Climate Model with thermosphere and ionosphere eXtension model (WACCM-X 2.1) to derive the horizontal structure of the ion convergence region (HSICR) to explore the shapes of the large-scale Es layers over East Asia for the period from June 1 to August 31, 2008. The simulation produced the various shapes of the HSICRs elongated in the northwest–southeast, northeast–southwest, or composed of individual small patches. The close connection between Es layer critical frequency ($f_o$Es) and vertical ion convergence indicates that the HSICR is a good candidate for revealing and explaining the horizontal structure of the large-scale Es layers.

**Keywords:** sporadic E layer; horizontal structure; wind shear; WACCM-X model

## 1. Introduction

Sporadic E (Es) layers are thin layers that occasionally form at altitudes between 95 and 125 km (e.g., Whitehead, 1961; Arras et al., 2008). They have a higher electron density than the E layer peak or even the F layer peak, and thus can severely interfere with long-distance radio communications and even cause the loss of radio signals (Yue XN et al., 2016). The observations and theoretical interpretations of Es layers have always been important for space weather and navigation communication.

Since Es layers appear randomly, their occurrence characteristics have been studied extensively over many years. A large number of observations have confirmed that the occurrence rate of Es layers has obvious seasonal and geographical dependence (e.g., Smith, 1978; Arras et al., 2008; Chu YH et al., 2014; Zhou C et al., 2017; Resende et al., 2018; Luo J et al., 2021; Liu ZD et al., 2021; Niu J, 2021; Sobhkhiz-Miandehi et al., 2022; Xu XH et al., 2022). Es layers occur mainly in the mid-latitude regions of the summer hemisphere. Moreover, Es layer activity exhibits regional preference. For example, Es layers appear relatively frequently over China and Japan, but rarely over North America and the South Atlantic (Arras et al., 2008; Chu YH et al., 2014).

The physics of mid-latitude Es layer formation has been described by the wind shear theory (Whitehead, 1961). The long-lived metallic ions ($Fe^+$, $Mg^+$) (Plane et al., 2015) are converged into a thin layer in the ionospheric E region by vertical shears (Yamazaki et al., 2023; Zhou BZ et al., 2022) in the horizontal neutral winds. The seasonal and geographic dependence of the occurrence of Es layers, which can be attributed to the combined interaction of global neutral wind shear and the geomagnetic field, has been well explained by simulations (Chu YH et al., 2014; Shinagawa et al., 2017; Yu BK et al., 2019; Qiu LH et al., 2019) and observations (Liu Y et al., 2018; Yamazaki et al., 2022).

In addition to their occurrence and distribution characteristics, the

First author: L. H. Qiu, qiulihui16@163.com
Correspondence to: T. Yu, yutaommnn@163.com
Received 25 APR 2023; Accepted 20 JUN 2023.
First Published online 14 JUL 2023.

horizontal structure of Es layers has drawn the attention of investigators. Rice et al. (2011) mapped the large-scale structure of Es layers scattered across the United States with a passive observing network of Space Weather–Aware Receiver Elements (SWAREs). Their experiment detected geographic extension, drift, and decay of Es layers over regions of several hundred kilometers. E region irregularities covering more than 300 km longitudinally are detected by all-sky meteor radar in China (Wang Y et al., 2019; Sun WJ et al., 2023). The 2D structure of the Es layer was further revealed by a dense network of Global Positioning System (GPS) receivers (e.g., Maeda and Heki, 2014, 2015; Sun WJ et al., 2018; Fu WZ et al., 2021). Maeda and Heki (2014), for the first time, used a dense GPS array in Japan to capture a strong Es layer event with an Es layer critical frequency ($f_o$Es) of ~22 MHz. The slender Es layer is ~150 km in east–west (E-W) and 30 km in north–south (N-S). Maeda and Heki (2015) further analyzed 70 events and concluded that Es layers can be elongated in the E-W and northeast–southwest (NE-SW) directions. Moreover, large-scale Es layers elongated 1000–3000 km in northwest–southeast (NW-SE) direction were observed by ground-based GNSS receivers in China (Sun WJ et al., 2018). After statistical analysis, Sun WJ et al. (2021) suggested that such large-scale strong Es layers appear mainly in summer and are elongated in the E-W and NW-SE directions.

It must be noted that, however, ground-based GNSS observation networks can reveal only part of the structure of strong Es layers ($f_o$Es > 14 MHz) (Sun WJ et al., 2018). GNSS total electron content (TEC) data cannot reveal the structure of Es layers with relatively low electron density. In fact, most Es layers have intensities below 10 MHz (Zhou C et al., 2017) and cannot even be detected by ground-based GNSS observation networks. Second, as mentioned above, Es layers do not exhibit a single horizontal orientation (Maeda and Heki, 2015; Sun WJ et al., 2021). They can be elongated in the NW-SE or the NE-SW directions.

Therefore, this paper aims to investigate whether or not the background neutral winds can form a large-scale ion convergence structure that supports the formation of an Es layer. We then further study the horizontal structure characteristics of the ion convergence regions. A primary difficulty in simulating their horizontal structures is the lack of continuous and wide-area atmosphere observations. In this work, to calculate the horizontal structure of ion convergence region (HSICR), we employ the Whole Atmosphere Community Climate Model with thermosphere and ionosphere eXtension model (WACCM-X) that can self-consistently simulate dynamic, physical, chemical, radiative, and atmospheric processes (Liu HL et al., 2018). The wind shear convergence calculation methods are introduced in Section 2. Section 3 presents examples and statistical features of HSICR. Sections 4 and 5 contain our discussions and conclusions, respectively.

## 2. Data and Methods

Based on the WACCM-X 2.1 model, we analyze the HSICR over East Asia (60°E–150°E and 10°N–60°N) for the period from June 1 to August 31, 2008. The WACCM-X is a numerical model developed by the National Center for Atmospheric Research. It can self-consistently resolve dynamic and physical processes from the surface to ~700 km altitude (Liu HL et al., 2018). Its inputs include the day of year, time of day, latitude, longitude, solar 10.7 cm radio flux index, and geomagnetic index *Kp*. A detailed description and validation of the WACCM-X model can be found in Liu HL et al. (2018). This study employs the free-running WACCM-X model that has a grid of 2.5° longitude by 1.9° latitude horizontally. The axes are *x* (positive southward), *y* (positive eastward), and *z* (positive upward). The Es layer is composed mainly of long-lived metal ions, such as $Fe^+$ and $Mg^+$. The vertical ion ($Fe^+$) velocity, $V_{iz}$, is written as (Whitehead, 1961)

$$V_{iz} = \frac{V\cos I\sin I + (\nu_i/\omega_i)U\cos I}{1+(\nu_i/\omega_i)^2}, \tag{1}$$

where $\nu_i/\omega_i$ is the ratio of the ion–neutral collision frequency to the ion gyrofrequency, $I$ is the magnetic inclination, and $V$ and $U$ are southward and eastward neutral winds, respectively.

The $\nu_i/\omega_i$ as a function of altitude is given by Nygrén et al. (1984) and Mathews (1998). Taking the $\nu_i/\omega_i$ over Wuhan (114.4°E, 30.5°N) as an example, as shown in Figure 1a, its value is 1 at around 123 km where the convergence efficiency of the zonal wind shear and meridional wind shear is equivalent. At altitudes above 123 km, the meridional wind, which moves ions along geomagnetic lines, works more efficiently. At heights below 123 km, the zonal wind shear mechanism becomes dominant (Haldoupis,

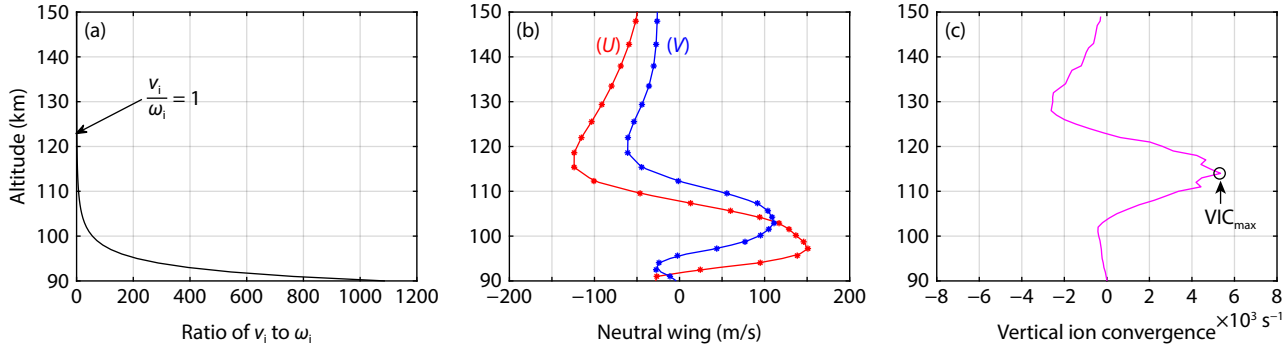


**Figure 1**. An example of the input parameters used to simulate the horizontal structure of the ion convergence region at 00:00 UT on July 25, 2008, over Wuhan (114.4°E, 30.5°N). (a) The altitude profile of the ratio of the ion–neutral collision frequency to the ion gyrofrequency. (b) The altitude profiles of zonal (*U*, red line) and meridional (*V*, blue line) winds. (c) The altitude profile of vertical ion convergence intensity (VIC). VIC > 0 represents ion convergence.

2011). The magnetic field parameters are obtained from the International Geomagnetic Reference Field (IGRF 11) model (Finlay et al., 2010). The neutral winds, $V$ and $U$, in the altitude range from 90 to150 km, are derived from the WACCM-X model. Figure 1b shows the zonal ($U$, red line) and meridional ($V$, blue line) winds at 00:00 UT on July 25, 2008, over Wuhan. Markers represent raw data derived from the WACCM-X model. The zonal (meridional) winds are eastward (southward) at low altitudes and westward (northward) at high altitudes, suggesting that there is a negative gradient in the vertical shear of neutral winds, which is favorable for the formation of Es layer.

The vertical ion convergence (VIC) can be represented by the gradient of ion vertical velocity (Shinagawa et al., 2017).

$$\mathrm{VIC} = \begin{cases} -\dfrac{\partial V_{iz}}{\partial z}, & \dfrac{\partial V_{iz}}{\partial z} < 0, \\ 0, & \dfrac{\partial V_{iz}}{\partial z} \geq 0, \end{cases} \tag{2}$$

where $z$ is the altitude. $-\dfrac{\partial V_{iz}}{\partial z} > 0$ indicates that the wind shear supports the formation of an Es layer. In this study we use the $\mathrm{VIC}_{max}$, as shown in Figure 1c, to represent the wind shear convergence capability at a fixed location. The horizontal structure of the ion convergence region can be revealed by calculating the $\mathrm{VIC}_{max}$ for each geographic location.

## 3. Results

### 3.1 Example of the HSICR

In this case, we have presented an example to give an intuitive image of the HSICR. Figure 2 (left panels) shows the contour maps of zonal winds at different altitudes over East Asia at 00:00 UT on July 25, 2008. On the one hand, there are eastward and westward winds exhibiting in different areas at a fixed altitude. On the other hand, the magnitudes and directions of the zonal winds change as the altitude increases from 106 km to 118 km. For example, the eastward winds dominate at low altitudes, while westward winds dominate at high altitudes. This suggests the existence of a convergent wind shear region that supports the formation of an Es layer. Similarly, Figure 2 (middle panels) also conforms to the meridional wind shear mechanism. There is a negative wind gradient from low to high altitudes, which supports the formation of an Es layer. Figure 2 (right panels) shows the VIC regions based on Equations (1) and (2). The VIC regions exhibit large-scale features characterized by frontal structures typically elongated in the NE-SW direction. The simulated VIC regions can cover around 10–40 degrees in the longitudinal direction.

Figure 3 displays the HSICR over East Asia at 00:00 UT on July 25, 2008. The HSICR shows a large-scale structure spanning about 50 degrees in longitude and 30 degrees in latitude. The shape of the HSICR is elongated in the NE-SW direction, as indicated by the white dashed line.

We used four ionosondes and Constellation Observing System for Meteorology, Ionosphere, and Climate (COSMIC-1) satellites to check for the presence of Es layers over East Asia. The geographical locations of the four ionosondes are indicated by pentagrams in Figure 3. The ground tracks of the tangent point locations of the observation profiles recorded by COSMIC at the altitude of 70–150 km are denoted by black short lines (a–l). We use S4 > 0.3 (scintillation index) and $f_o$Es > 3 MHz to check for the existence of an Es layer (Qiu LH et al., 2021a, b). Figure 4 shows that all S4 observation profiles (a–l) display strong enhancement at 100–110 km altitudes. Furthermore, all S4max given in Table 1 are greater than 0.3, which means that the Es layers are likely to be recorded in these occultation events. At the same time, the $f_o$Es recorded by the four ionosondes also exceeded 3 MHz. These observations indicate that there may be an Es layer covering 90–150 degrees in longitude and 15–40 degrees in latitude. In addition, the ion convergence region covers most of the observed tracks, suggesting that the HSICR plays a key role in the layout of an Es layer.

### 3.2 Statistical Results

First, using data from the two ionosonde instruments located in Beijing and Wuhan, we examined the wind shear theory and confirmed that there is a close connection between the Es layer and vertical ion convergence. Second, we analyzed statistically the shapes and horizontal orientations of HSICRs derived from the WACCM-X model for the period from June 1 to August 31, 2008.

Figure 5 display the mean daily variation of $f_o$Es and $\mathrm{VIC}_{max}$ based on these three months of data. The red and blue lines represent the $f_o$Es recorded by ionosondes and the $\mathrm{VIC}_{max}$ derived from WACCM-X, respectively. Both the observed $f_o$Es and the simulated $\mathrm{VIC}_{max}$ have daily two peaks over Wuhan (Figure 5a) and Beijing (Figure 5b). One peak is around 2:00 UT and the other peak is around 15:00 UT. The agreement between the $f_o$Es and $\mathrm{VIC}_{max}$ suggests that the vertical neutral wind shear is a major factor in the formation of Es layers.

The features of HSICRs at 2:00 and 15:00 UT were statistically analyzed. Based on the characteristics of shape and horizontal orientations, the results are classified into four categories: HSICR elongated in NW-SE (A type), HSICR elongated in NE-SW (B type), HSICR of indeterminate shape (C type), HSICR exhibiting no vertical ion convergence (D type). Figure 6a shows the A-type HSICR appearing in the range of 70°E–100°E and 10°N–35°N. Figure 6b displays the B-type HSICR. Figure 6c displays the C-type HSICR, which has multiple ion convergence regions with different horizontal orientations. Figure 6d shows the D-type HSICR with very low VIC, which does not support the formation of Es layers.

Figure 7 is a histogram showing the frequency of each of the four categories of ion convergence region at the two daily peak times. Red indicates HSICR type counts at 2:00. Blue indicates counts at 15:00 UT. First, 77% of these events exhibit high vertical ion convergence, capable of supporting Es layer formation (A, B, C types). 23% of them (D type) do not meet the required conditions. Second, of those with high vertical ion convergence, the orientation of 63% is horizontal. Third, the events without ion convergence (D type) are more frequent at 15:00 UT (night time; LT = UT + 8) than that at 2:00 UT (day time). This is because the wind shear intensity at 15:00 UT is weaker than that at 2:00 UT (Figure 5), which agrees with previous results obtained from the HWM14 model (Qiu LH et al., 2021a).

Figure 8 displays the horizontal orientations of HSICRs (A and B

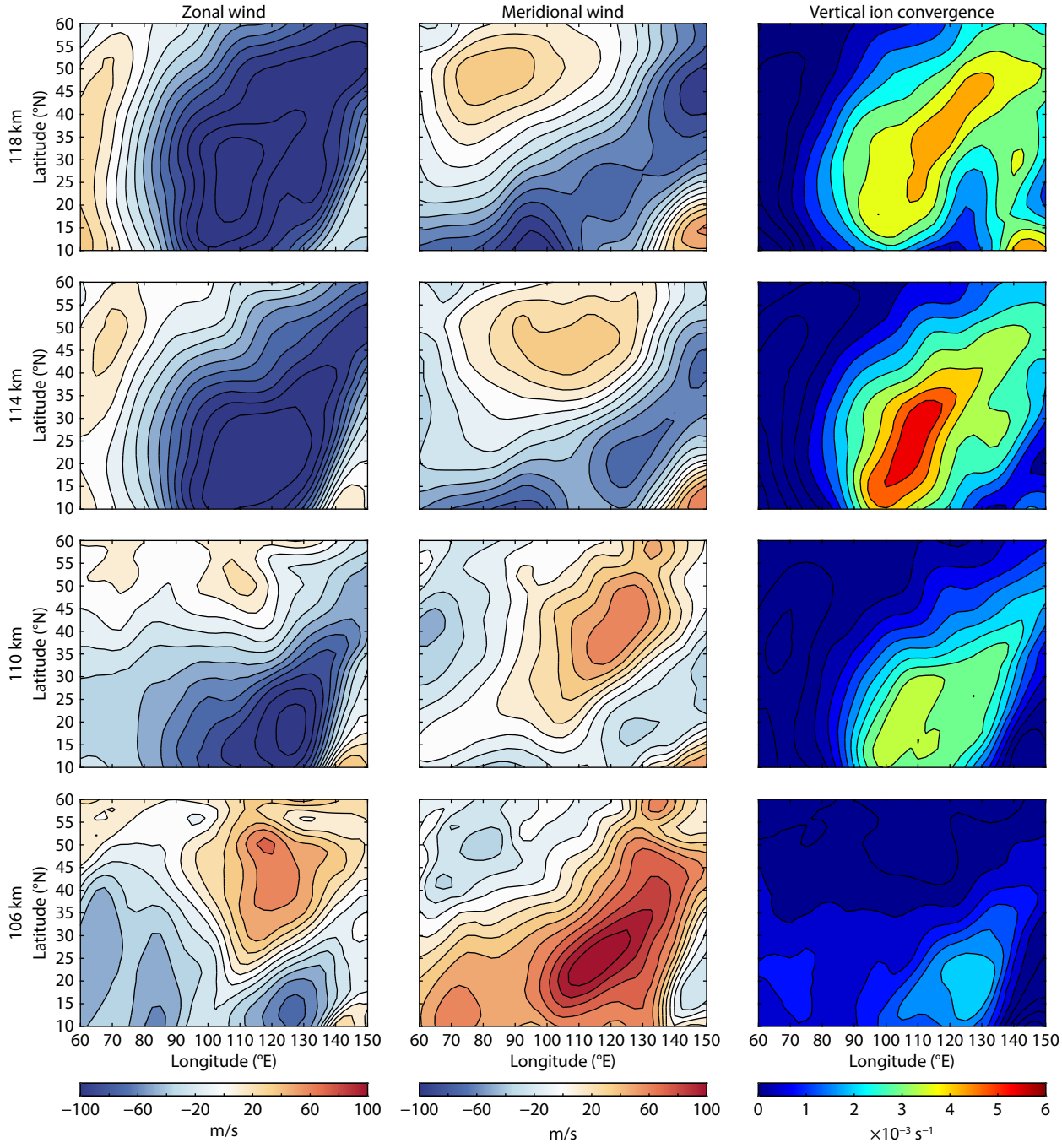


**Figure 2**. Contour maps of zonal (left panels) and meridional (middle panels) winds at different altitudes over East Asia at 00:00 UT on July 25, 2008. The eastward and southward are positive, respectively. (Right panels) Horizontal structures of vertical ion convergence regions.

types). The black lines represent the fronts of HSICRs. Figures 8a and 8c display the A-type HSICRs superimposed on the map at 2:00 and at 15:00 UT, respectively. The HSICRs show frontal structures elongated in NW-SE direction, spanning around 90°E–120°E and 10°N–40°N. Figures 8b and 8d show the B-type HSICRs at 2:00 and 15:00 UT, respectively. The HSICRs are characterized by their frontal structures, appearing mainly around 90°E–130°E and 10°N–40°N, elongated in NE-SW direction.

## 4. Discussion

The formation of Es layers is related mainly to neutral winds, geomagnetic fields, metallic ions, and electric fields (Whitehead, 1961; Nygrén et al., 1984; Arras et al., 2013; Andoh et al., 2022). Of these, vertical wind shear and magnetic fields are the main factors controlling the dynamic process of Es layer formation in the mid-latitudes. The electric field is the main factor in equatorial Es layer formation (Abdu et al., 2014; Moro et al., 2017). In this study, we focus on the East Asia area (60°E–150°E and 10°N–60°N). The vertical $Fe^+$ velocity,

$$V_{iz} = \frac{1}{\left(\frac{\nu_i}{\omega_i}\right)^2 + 1}\left(U_x \sin\theta\cos\theta + \left(\frac{\nu_i}{\omega_i}\right)U_y\cos\theta\right),$$

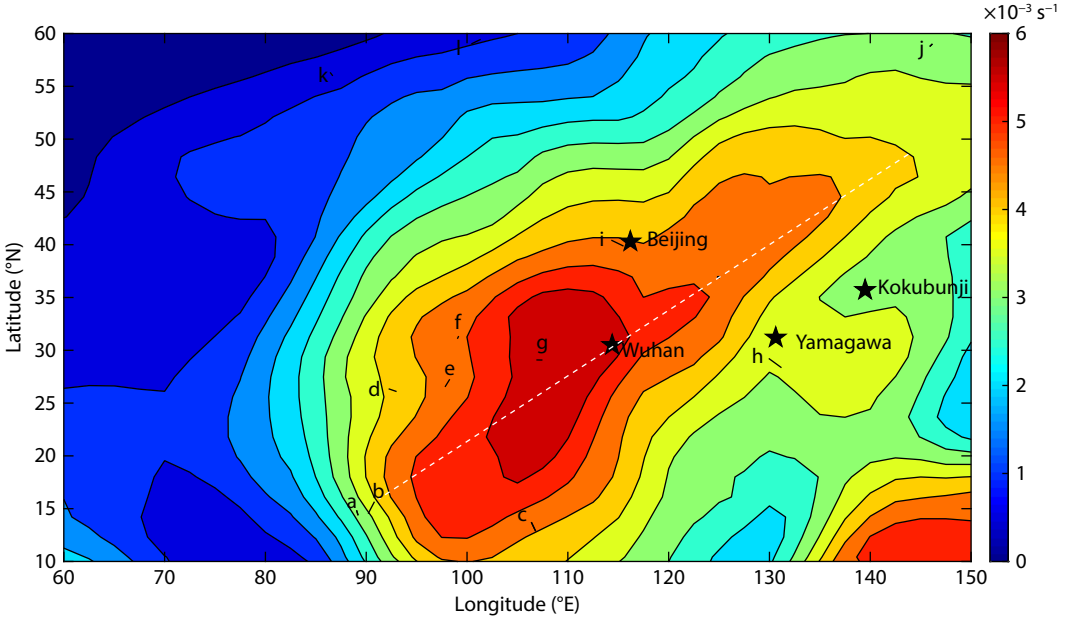


**Figure 3**. The horizontal structure of the ion convergence region (HSICR) over East Asia at 00:00 UT on July 25, 2008. The pentagrams represent the four ionosondes located at Wuhan, Beijing, Yamagawa, and Kokubunji, respectively. The black short lines (a–l) indicate the ground tracks of the tangent point locations of the observation profiles recorded by Constellation Observing System for Meteorology, Ionosphere, and Climate (COSMIC-1). The white dashed line represents the orientation of the HSICR.

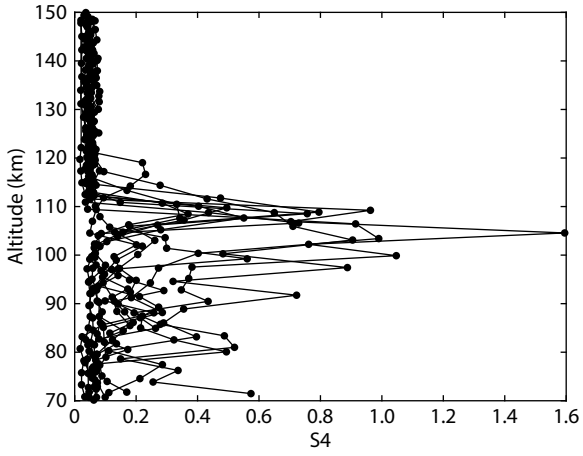


**Figure 4**. The scintillation index (S4) profiles obtained from the Constellation Observing System for Meteorology, Ionosphere, and Climate (COSMIC-1) satellites around 00:00 UT on July 25, 2008.

**Table 1.** Basic parameters of the ionosondes and radio occultation profiles used in Figure 3.

| Stations and tracks | Longitude | Latitude | UT (h) | $f_o$Es and S4max |
|---|---|---|---|---|
| Beijing | ~116°E | ~40°N | 00:00 | 6.32 MHz |
| Wuhan | ~114°E | ~30°N | 00:00 | 3.99 MHz |
| Yamagawa | ~131°E | ~31°N | 00:00 | 4.88 MHz |
| Kokubunji | ~140°E | ~36°N | 00:00 | 3.60 MHz |
| a | ~89°E | ~15°N | 23:56 | 0.55 |
| b | ~90°E | ~15°N | 00:29 | 0.73 |
| c | ~107°E | ~13°N | 23:44 | 0.37 |
| d | ~93°E | ~26°N | 00:14 | 0.76 |
| e | ~98°E | ~27°N | 00:08 | 0.50 |
| f | ~99°E | ~31°N | 00:13 | 0.34 |
| g | ~107°E | ~29°N | 00:02 | 0.90 |
| h | ~131°E | ~29°N | 00:08 | 0.56 |
| i | ~115°E | ~40°N | 00:24 | 1.59 |
| j | ~146°E | ~58°N | 23:29 | 0.98 |
| k | ~86°E | ~56°N | 00:05 | 0.49 |
| l | ~100°E | ~59°N | 00:53 | 0.79 |

mainly depends on the neutral winds and magnetic fields.

The simulation results in this study show the various shapes of HSICRs. The shapes of HSICRs can be elongated in the NW-SE (Figure 6a), NE-SW (Figure 6b), or can occur in a broad area composed of individual patches (Figure 6c). Besides, the histogram of the angles between the north direction and the HSICR fronts (black lines in Figure 8) is also shown in Figure 9a. Clockwise is positive. It can further indicate that the dominant orientations of HSICRs are NW-SE and NE-SW. Using the dense GNSS observation networks over China, Sun WJ et al. (2021) revealed that the most Es layers are elongated in NW-SE (Figure 9b), which mainly consistent with A-type HSICRs. Maeda and Heki (2015), using the dense GPS observation networks in Japan, showed that the Es layers are elongated in NE-SW and E-W, which are agree with the B-type HSICRs. Andoh et al. (2021) simulated several events for the temporal evolution of 3-D structures of metal ions layers, and their results also agree with our A, B, and C-type HSICRs. However, due to the inconsistency of the previous observation results, more observations and simulations (i.e.,

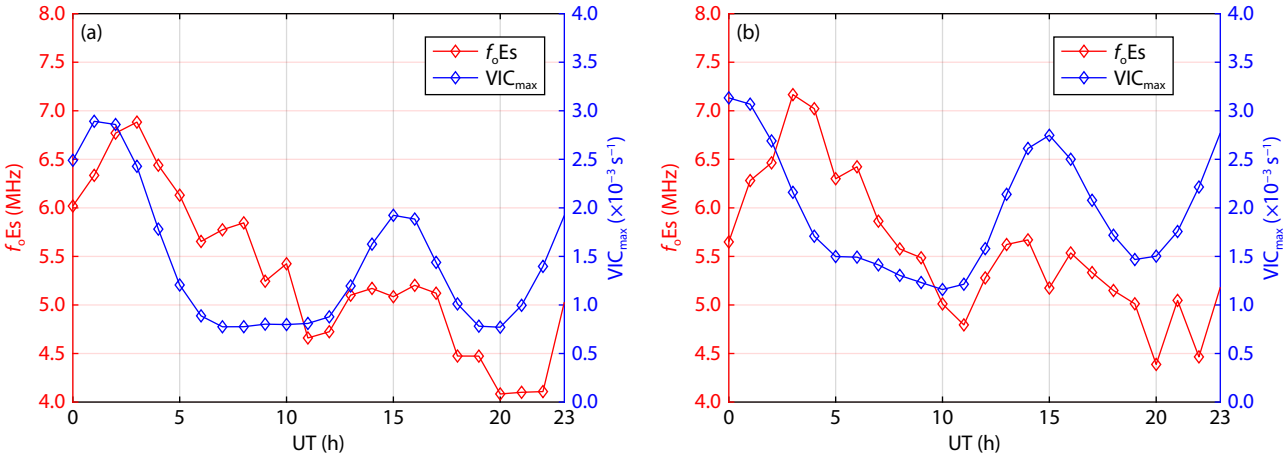


**Figure 5**. Comparisons of the VIC$_{max}$ derived from WACCM-X and the $f_o$Es recorded by the ionosondes at (a) Wuhan and (b) Beijing, respectively. (VIC = vertical ion convergence).

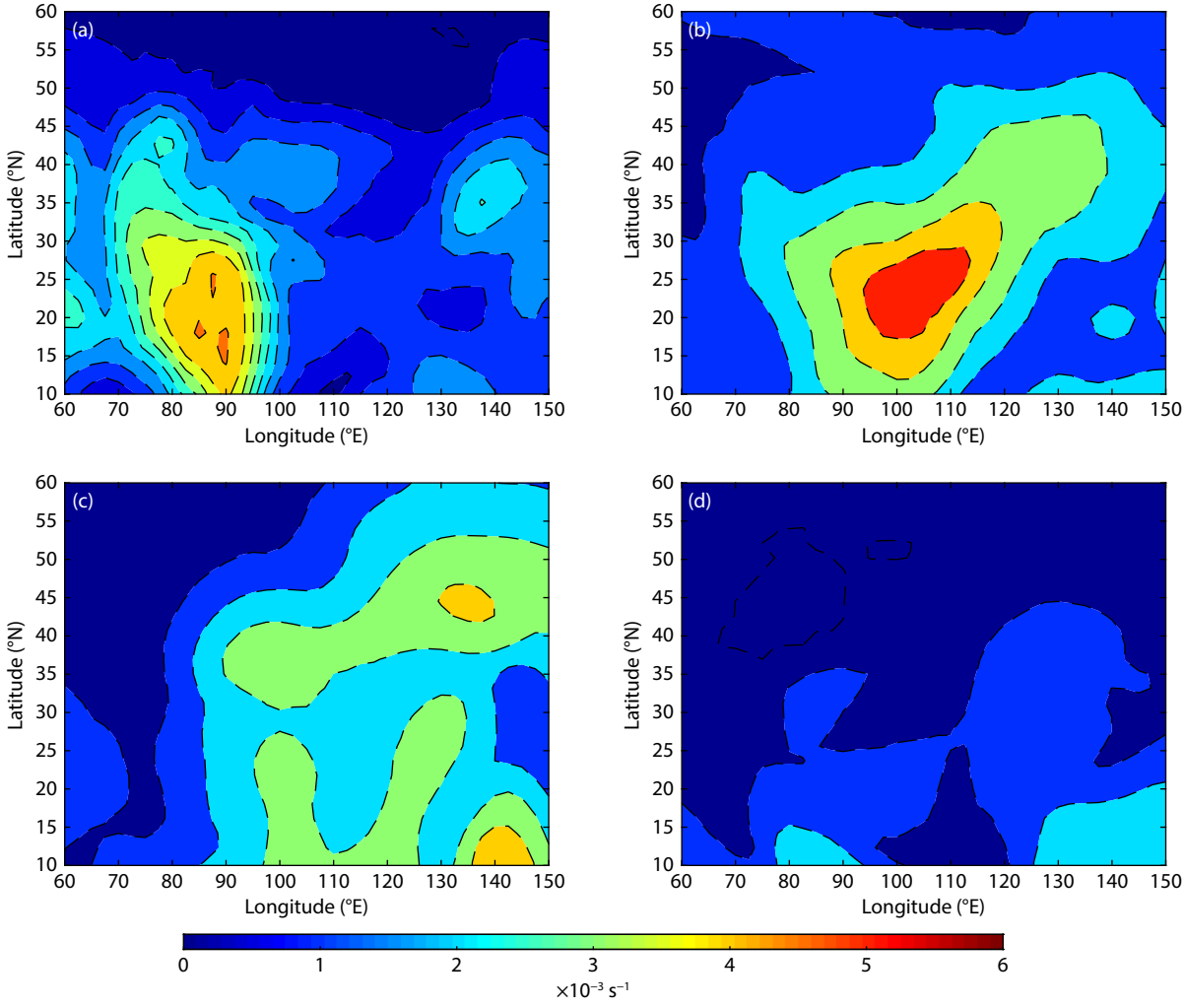


**Figure 6**. Four examples of horizontal structure of ion convergence regions (HSICRs). (a) HSICR elongated in the northwest–southeast (A type). (b) HSICR elongated in the northeast–southwest (B type). (c) HSICR exhibiting multiple ion convergence regions with indeterminate horizontal orientations (C type). (d) HSIR exhibiting no vertical ion convergence (D type).

America sector, several years of data) need to be further carried out to find out the horizontal structures of Es layers.

Although the Es layers recorded by the ground-based GNSS observation networks are long strip-like shapes, they are very narrow and look very slender (Maeda and Heki, 2015; Sun WJ et al., 2021). The simulated HSICRs (Figure 3) are also elongated but appear relatively wider than the Es layers recorded by the ground-based GNSS observation networks. The reason is that ground-based GNSS observation networks can detect only the stronger Es layers ($f_o$Es > 14 MHz) (Sun WJ et al., 2018) and thus cannot reveal the edge structure of Es layers with relatively low electron density. Essentially, ground-based GNSS observation networks show only a small portion of Es layers. Deacon et al. (2022) demonstrated a full-scale Es layer case based on amateur radio signal reports. The Es layer extended along the NE-SW direction and was relatively wide, which agrees well with the HSICR shown in Figure 3.

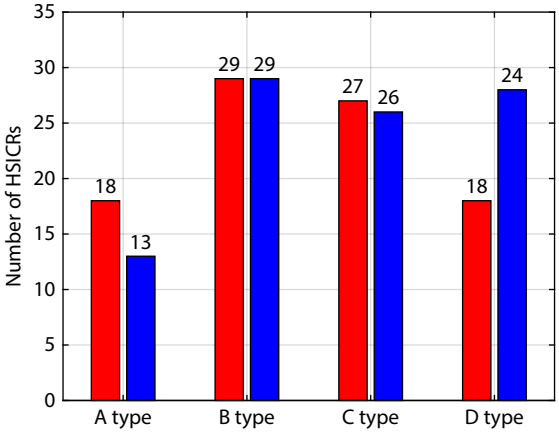


**Figure 7**. Histogram of the four categories of ion convergence region. Red and blue represent the numbers of each type of horizontal structure of ion convergence region (HSICR) at 2:00 and 15:00 UT, respectively.

In addition to the HSICRs elongated in the NW-SE and NE-SW, some HSICRs lack specific horizontal orientation (Figure 6c). These HSICRs may consist of multiple small-scale convergent regions. This means that scattered Es layers can appear randomly in different geographical areas, which may be one reason why Es layers appear sporadically. Rice et al. (2011) detected Es layers using oblique HF propagation from existing transmitters. The observing network showed that an Es layer can rapidly appear or disappear over an area of several hundred kilometers.

The HSICR is a good reference for revealing the horizontal structure of an Es layer, especially when direct observation of the layer's

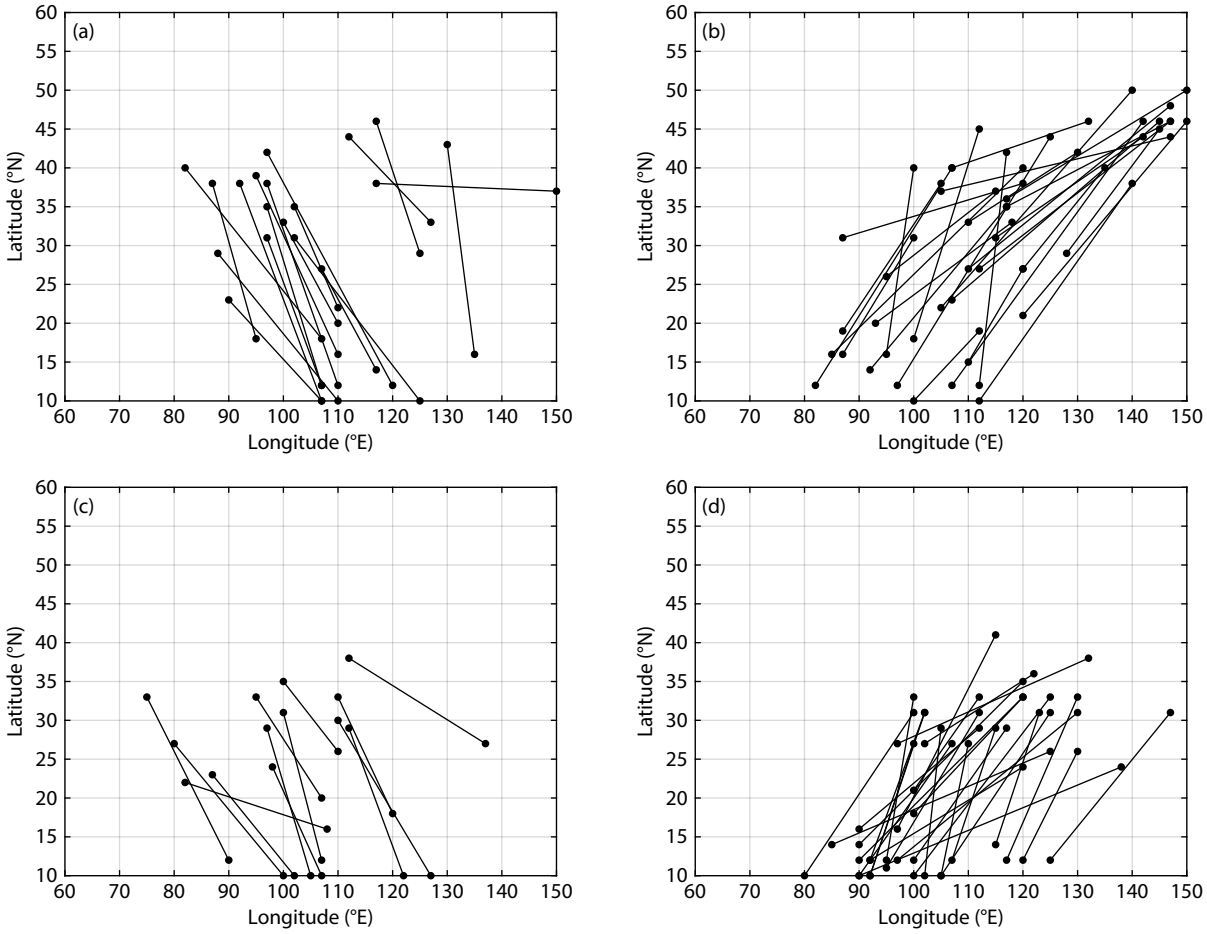


**Figure 8**. Orientations of the horizontal structures of ion convergence regions (HSICRs. A-type HSICR elongated in the northwest–southeast; B-type HSICR elongated in the northeast–southwest. (a and c) A-type HSICRs at 2:00 and 15:00 UT, respectively. (b and d) B-type HSICRs at 2:00 and 15:00 UT, respectively.

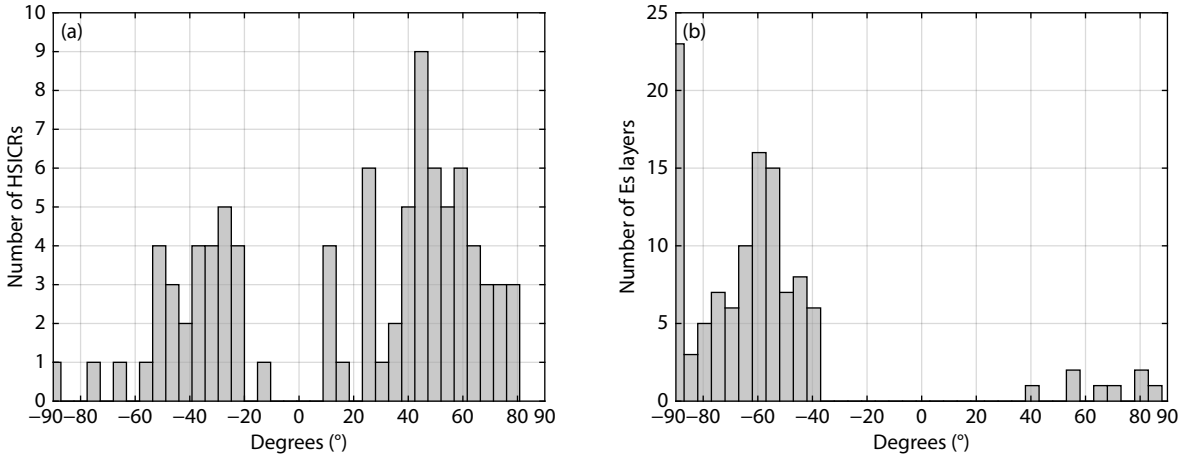


**Figure 9**. (a) Histogram of angles between the north direction and the HSICR (horizontal structure of ion convergence region) fronts. (b) Histogram of angles between the north direction and the orientation of Es layers observed by the ground-based GNSS observation networks (Sun WJ et al., 2021). Clockwise is positive.

horizontal structure is lacking. The agreement between $f_o$Es and VIC (Figure 5) also indicates that vertical ion convergence is a major factor in controlling the occurrence and disappearance of Es layers. However, the neutral wind shear is not the only factor driving formation of Es layers. The VIC has an obvious peak around 15:00 UT, but the $f_o$Es peak at that time is weak (Figure 5b). Es layers can be modulated also by background metallic ion distribution and gravity waves (Hocke and Tsuda, 2001; Didebulidze et al., 2020; Chen G et al., 2021; Wang J et al., 2021) connected with tropospheric convective activities. The impacts of metallic ion distribution and gravity waves on the Es layer structure and formation need to be studied in the future. In addition, day-to-day variability of HSICRs needs to be further investigated by using the WACCM-X model nudged by the MERRA-2 data reanalysis method (Modern-Era Retrospective analysis for Research and Applications, version 2, Bosilovich et al., 2015). Moreover, the roles played in the formation of HSICRs by various tidal components and the interaction of tides with other large-scale waves need to be distinguished.

## 5. Conclusion

This study investigated the HSICRs over East Asia by using the WACCM-X model applied to the period from June 1 to August 31, 2008. The simulation produced HSICRs elongated in the NW-SE, in the NE-SW, or composed of individual small patches. These elongated HSICRs have large scales of 10–30 degrees in longitude, which agrees with horizontal structures derived from Es layer data from ground-based GNSS observation networks and amateur radio signal reports. The good agreement between $f_o$Es and $VIC_{max}$ indicates that the large-scale shapes of Es layers can be explained through the geographic distribution of HSICRs.

## Data Availability statement

The WACCM-X model source code can be found at (https://www2.hao.ucar.edu/modeling/waccm-x). The F3/C data were provided by the COSMIC Data Analysis and Archival Center and the Taiwan Analysis Center for COSMIC (https://cdaac-www.cosmic.ucar.edu/). The ionosonde data analyzed in this paper are available at: https://giro.uml.edu/didbase/scaled.php, Space Weather, Tokyo, National Institute of Information and Communications Technology (https://wdc.nict.go.jp/IONO/HP2009/ISDJ/index-E.html), and Beijing National Observatory of Space Environment, Institute of Geology and Geophysics, Chinese Academy of Science (http://geospace.geodata.cn/index.html).

## Acknowledgments

This research is supported by the Strategic Priority Research Program of the Chinese Academy of Sciences (Grant No. XDA17010207). We thank Wenjie Sun for providing the coordinate data of the Es layers recorded by the ground-based GNSS receiver networks. Lihui Qiu thanks the scholarship received from the China Scholarship Council (CSC) under grant CSC No.202006410017. The project was supported by the Fundamental Research Funds for National University, China University of Geosciences (Wuhan). We thank the Data Center for Meridian Space Weather Monitoring Project and Beijing National Observatory of Space Environment, Institute of Geology and Geophysics, Chinese Academy of Sciences.

## References

Abdu, M. A., De Souza, J. R., Batista, I. S., Santos, A. M., Sobral, J. H. A., Rastogi, R. G., and Chandra, H. (2014). The role of electric fields in sporadic *E* layer formation over low latitudes under quiet and magnetic storm conditions. *J. Atmos. Solar-Terr. Phys.*, *115–116*, 95–105. https://doi.org/10.1016/j.jastp.2013.12.003

Andoh, S., Saito, A., and Shinagawa, H. (2021). Temporal evolution of three-dimensional structures of metal ion layer around Japan simulated by a midlatitude ionospheric model. *J. Geophys. Res.: Space Phys.*, *126*(6), e2021JA029267. https://doi.org/10.1029/2021JA029267

Andoh, S., Saito, A., and Shinagawa, H. (2022). Numerical simulations on day-to-day variations of low-latitude Es layers at Arecibo. *Geophys. Res. Lett.*, *49*(7), e2021GL097473. https://doi.org/10.1029/2021GL097473

Arras, C., Wickert, J., Beyerle, G., Heise, S., Schmidt, T., and Jacobi, C. (2008). A global climatology of ionospheric irregularities derived from GPS radio occultation. *Geophys. Res. Lett.*, *35*(14), L14809. https://doi.org/10.1029/2008GL034158

Arras, C., Wickert, J., Jacobi, C., Beyerle, G., Heise, S., and Schmidt, T. (2013). Global sporadic *E* layer characteristics obtained from GPS radio occultation

measurements. In F. J. Lübken (Ed.), *Climate and Weather of the Sun-Earth System (CAWSES)* (pp. 207-221). Dordrecht: Springer. https://doi.org/10.1007/978-94-007-4348-9_12

Bosilovich, M. G., Akella, S., Coy, L., Cullather, R., Draper, C., Gelaro, R., et al. (2015). MERRA-2: Initial evaluation of the climate. NASA technical report series on global modeling and data assimilation. NASA/TM-2015-104606. (Vol. 43). Goddard Space Flight Center. https:// gmao.gsfc.nasa.gov/reanalysis/MERRA-2/docs

Chen, G. Wang, J., Reinisch, B. W., Li, Y., and Gong, W. (2021). Disturbances in Sporadic-E during the great solar eclipse of August 21, 2017. *J. Geophys. Res.: Space Phys.*, *126*(5), e2020JA028986. https://doi.org/10.1029/2020JA028986

Chu, Y. H., Wang, C. Y., Wu, K. H., Chen, K. T., Tzeng, K. J., Su, C. L., Feng, W., and Plane, J. M. C. (2014). Morphology of sporadic *E* layer retrieved from COSMIC GPS radio occultation measurements: wind shear theory examination. *J. Geophys. Res.: Space Phys.*, *119*(3), 2117–2136. https://doi.org/10.1002/2013JA019437

Deacon, C., Mitchell, C., and Watson, R. (2022). Consolidated amateur radio signal reports as indicators of intense sporadic E layers. *Atmosphere*, *13*(6), 906. https://doi.org/10.3390/atmos13060906

Didebulidze, G. G., Dalakishvili, G., and Todua, M. (2020). Formation of Multilayered sporadic E under an influence of atmospheric gravity waves (AGWs). *Atmosphere*, *11*(6), 653. https://doi.org/10.3390/atmos11060653

Finlay, C. C., Maus, S., Beggan, C. D., Bondar, T. N., Chambodut, A., Chernova, T. A., Chulliat, A., Golovkov, V. P., Hamilton, B., … Zvereva, T. I. (2010). International geomagnetic reference field: The eleventh generation. *Geophys. J. Int.*, *183*(3), 1216–1230. https://doi.org/10.1111/j.1365-246X.2010.04804.x

Fu, W. Z., Ssessanga, N., Yokoyama, T., and Yamamoto, M. (2021). High-resolution 3-D imaging of daytime sporadic-E over Japan by using GNSS TEC and ionosondes. *Space Wea.*, *19*(12), e2021SW002878. https://doi.org/10.1029/2021SW002878

Haldoupis, C. (2011). A tutorial review on sporadic *E* layers. In M. A. Abdu, et al. (Eds.), *Aeronomy of the Earth's Atmosphere and Ionosphere* (pp. 381-394). Dordrecht: Springer. https://doi.org/10.1007/978-94-007-0326-1_29

Hocke, K., and Tsuda, T. (2001). Gravity waves and Ionospheric irregularities over tropical convection zones observed by GPS/MET radio occultation. *Geophys. Res. Lett.*, *28*(14), 2815–2818. https://doi.org/10.1029/2001GL013076

Liu, H. L., Bardeen, C. G., Fosterr, B. T., Lauritzen, P., Liu, J., Lu, G., Marsh, D. R., Maute, A., McInerney, J. M., … Wang, W. B. (2018). Development and validation of the Whole Atmosphere Community Climate Model with thermosphere and ionosphere extension (WACCM-X 2.0). *J. Adv. Model. Earth Syst.*, *10*(2), 381–402. https://doi.org/10.1002/2017MS001232

Liu, Y., Zhou, C., Tang, Q., Li, Z. Q., Song, Y., Qing, H., Ni, B. B., and Zhao, Z. Y. (2018). The seasonal distribution of sporadic E layers observed from radio occultation measurements and its relation with wind shear measured by TIMED/TIDI. *Adv. Space Res.*, *62*(2), 426–439. https://doi.org/10.1016/j.asr.2018.04.026

Liu, Z. D., Fang, H. X., Yue, X. N., and Lyu, H. J. (2021). Wavenumber-4 patterns of the sporadic E over the middle- and low-latitudes. *J. Geophys. Res.: Space Phys.*, *126*(8), e2021JA029238. https://doi.org/10.1029/2021JA029238

Luo, J., Liu, H. F., and Xu, X. H. (2021). Sporadic E morphology based on COSMIC radio occultation data and its relationship with wind shear theory. *Earth, Planets Space*, *73*(1), 212. https://doi.org/10.1186/s40623-021-01550-w

Maeda, J., and Heki, K. (2014). Two-dimensional observations of midlatitude sporadic *E* irregularities with a dense GPS array in Japan. *Radio Sci.*, *49*(1), 28–35. https://doi.org/10.1002/2013RS005295

Maeda, J., and Heki, K. (2015). Morphology and dynamics of daytime mid-latitude sporadic-E patches revealed by GPS total electron content observations in Japan. *Earth Planets Space*, *67*(1), 89. https://doi.org/10.1186/s40623-015-0257-4

Mathews, J. D. (1998). Sporadic E: Current views and recent progress. *J. Atmos. Solar-Terr. Phys.*, *60*(4), 413–435. https://doi.org/10.1016/S1364-6826(97)00043-6

Moro, J., Resende, L. C. A., Denardini, C. M., Xu, J., Bstista, I. S., Andrioli, V. F., Carrasco, A. J., Batista, P. P., and Schuch, N. J. (2017). Equatorial *E* region electric fields and sporadic *E* layer responses to the recovery phase of the November 2004 geomagnetic storm. *J. Geophys. Res.: Space Phys.*, *122*(12), 12517–12533. https://doi.org/10.1002/2017JA024734

Niu, J. (2021). Relationship between wavenumber 4 pattern of sporadic E layer intensity and eastward propagating diurnal tide with zonal wavenumber 3 in low latitude region. *J. Geophys. Res.: Space Phys.*, *126*(6), e2020JA028985. https://doi.org/10.1029/2020JA028985

Nygrén, T., Jalonen, L., Oksman, J., and Turunen, T. (1984). The role of electric field and neutral wind direction in the formation of sporadic *E*-layers. *J. Atmos. Terr. Phys.*, *46*(4), 373–381. https://doi.org/10.1016/0021-9169(84)90122-3

Plane, J. M. C., Wuhu, Feng, and Dawkins, E. C. M. (2015). The mesosphere and metals: Chemistry and Changes. *Chem. Rev.*, *115*(10), 4497–4541. https://doi.org/10.1021/cr500501m

Qiu, L. H., Zuo, X. M., Yu, T., Sun, Y. Y., and Qi, Y. F. (2019). Comparison of global morphologies of vertical ion convergence and sporadic E occurrence rate. *Adv. Space Res.*, *63*(11), 3606–3611. https://doi.org/10.1016/j.asr.2019.02.024

Qiu, L. H., Zuo, X. M., Yu, T., Sun, Y. Y., Liu, H. X., Sun, L. F., and Zhao, B. Q. (2021a). The characteristics of summer descending sporadic E layer observed with the ionosondes in the China region. *J. Geophys. Res.: Space Phys.*, *126*(3), e2020JA028729. https://doi.org/10.1029/2020JA028729

Qiu, L. H., Yu, T., Yan, X. X., Sun, Y. Y., Zuo, X. M., Yang N., Wang, J., and Qi, Y. F. (2021b). Altitudinal and latitudinal variations in Ionospheric Sporadic-E layer obtained from FORMOSAT-3/COSMIC radio occultation. *J. Geophys. Res.: Space Phys.*, *126*(9), e2021JA029454. https://doi.org/10.1029/2021JA029454

Resende, L. C. A., Arras, C., Batista, I. S., Denardini, C. M., Bertollotto, T. O., and Moro, J. (2018). Study of sporadic E layers based on GPS radio occultation measurements and digisonde data over the Brazilian region. *Ann. Geophys.*, *36*(2), 587–593. https://doi.org/10.5194/angeo-36-587-2018

Rice, D. D., Sojka, J. J., Eccles, J. V., Raitt, J. W., Barday, J. J., and Hunsucker, R. D. (2011). First results of mapping sporadic *E* with a passive observing network. *Space Wea.*, *9*(12), s12001. https://doi.org/10.1029/2011SW000678

Shinagawa, H., Miyoshi, Y., Jin, H., and Fujiwara, H. (2017). Global distribution of neutral wind shear associated with sporadic *E* layers derived from GAIA. *J. Geophys. Res.: Space Phys.*, *122*(4), 4450–4465. https://doi.org/10.1002/2016JA023778

Smith, E. K. (1978). Temperate zone sporadic-*E* maps ($f_oE_s$>7MHz). *Radio Sci.*, *13*(3), 571–575. https://doi.org/10.1029/RS013i003p00571

Sobhkhiz-Miandehi, S., Yamazaki, Y., Arras, C., Miyoshi, Y., and Shinagawa, H. (2022). Comparison of the tidal signatures in sporadic E and vertical ion convergence rate, using FORMOSAT-3/COSMIC radio occultation observations and GAIA model. *Earth, Planets Space*, *74*(1), 88. https://doi.org/10.1186/s40623-022-01637-y

Sun, W. J., Ning, B. Q., Yue, X. N., Li, G. Z., Hu, L. H., Chang, S. M., Lan, J. P., Zhu, Z. P., Zhao, B. Q., and Lin, J. (2018). Strong sporadic *E* occurrence detected by ground-based GNSS. *J. Geophys. Res.: Space Phys.*, *123*(4), 3050–3062. https://doi.org/10.1002/2017JA025133

Sun, W. J., Zhao, X. K., Hu, L. H., Yang, S. P., Xie, H. Y., Chang, S. M., Ning, B. Q., Li, J. Y., Liu, L. B., and Li, G. Z. (2021). Morphological characteristics of thousand-kilometer-scale Es structures over China. *J. Geophys. Res.: Space Phys.*, *126*(2), e2020JA028712. https://doi.org/10.1029/2020JA028712

Sun, W. J., Li, G. Z., Wang, Y., Hu, L. H., Xie, H. Y., Li, Y., Zhao, X. K., Ning, B. Q., and Liu, L. B. (2023). On the spatial structure and zonal drift of low latitude E region irregularity patches over Hainan. *J. Geophys. Res.: Space Phys.*, *128*(1), e2022JA031005. https://doi.org/10.1029/2022JA031005

Wang, J., Zuo, X. M., Sun, Y. Y., Yu, T., Wang, Y. G., Qiu, L. H., Mao, T., Yan, X. X., Yang, N., … Zhao, B. Q. (2021). Multilayered sporadic-*E* response to the annular solar eclipse on June 21, 2020. *Space Wea.*, *19*(3), e2020SW002643. https://doi.org/10.1029/2020SW002643 https://doi.org/10.1029/2020SW002643

Wang, Y., Li, G. Z., Ning, B. Q., Yang, S. P., Sun, W. J., and Yu, Y. (2019). All-Sky interferometric meteor radar observations of zonal structure and drifts of low-latitude ionospheric E region irregularities. *Earth Space Sci.*, *6*(12), 2653–2662. https://doi.org/10.1029/2019EA000884

Whitehead, J. D. (1961). The formation of the sporadic-E layer in the temperate zones. *J. Atmos. Terr. Phys.*, *20*(1), 49–58. https://doi.org/10.1016/0021-9169(61)90097-6

Xu, X. H., Luo, J., Wang, H., Liu, H. F., and Hu, T. Y. (2022). Morphology of sporadic E layers derived from Fengyun-3C GPS radio occultation measurements. *Earth, Planets Space*, *74*(1), 55. https://doi.org/10.1186/s40623-022-01617-2

Yamazaki, Y., Arras, C., Andoh, S., Miyoshi, Y., Shinagawa, H., Harding, B. J., Englert, C. R., Immel, T. J., Sobhkhiz-Miandehi, S., and Stolle, C. (2022). Examining the wind shear theory of sporadic E with ICON/MIGHTI winds and COSMIC-2 radio occultation data. *Geophys. Res. Lett.*, *49*(1), e2021GL096202. https://doi.org/10.1029/2021GL096202

Yamazaki, Y., Harding, B. J. Qiu, L. Stolle, C., Siddiqui, T. A., Miyoshi, Y., Englert, C. R., and England, S. L. (2023). Monthly climatologies of zonal-mean and tidal winds in the thermosphere as observed by ICON/MIGHTI during April 2020-March 2022. *Earth and Space Science*, 10 (6), e2023EA002962. https://doi.org/10.1029/2023EA002962

Yu, B. K., Xue, X. H., Yue, X. A., Yang, C. Y., Yu, C., Dou, X. K., Ning, B. Q., and Hu, L. H. (2019). The global climatology of the intensity of the ionospheric sporadic *E* layer. *Atmos. Chem. Phys.*, *19*(6), 4139–4151. https://doi.org/10.5194/acp-2018-790

Yue, X. N., Schreiner, W. S., Pedatella, N. M., and Kuo, Y. H. (2016). Characterizing GPS radio occultation loss of lock due to ionospheric weather. *Space Wea.*, *14*(4), 285–299. https://doi.org/10.1002/2015SW001340

Zhou, C., Tang, Q., Song, X. X., Qing, H., Liu, Y., Wang, X., Gu, X. D., Ni, B. B., and Zhao, Z. Y. (2017). A statistical analysis of sporadic *E* layer occurrence in the midlatitude China region. *J. Geophys. Res.*: *Space Phys.*, *122*(3), 3617–3631. https://doi.org/10.1002/2016JA023135

Zhou, B. Z., Xue, X. H., Yi, W., Ye, H. L., Zeng, J., Chen, J. S., Wu, J. F., Chen, T. D., and Dou, X. K. (2022). A comparison of MLT wind between meteor radar chain data and SD-WACCMX results. *Earth Planet. Phys.*, *6*(5), 451–464. https://doi.org/10.26464/epp2022040